

Determination of MHD mode structures using a soft X-ray diagnostics in TCV

M.B. Dreval^{1,2}, S.E. Sharapov³, M. Vallar⁴, B. Labit⁴, A.N. Karpushov⁴, M. Garcia-Munoz⁵, and TCV team[†]

¹ *Institute of Plasma Physics, National Science Center, Kharkov Institute of Physics and Technology, 61108 Kharkov, Ukraine*

² *V.N. Karazin Kharkiv National University, Kharkiv, Ukraine*

³ *Culham Centre for Fusion Energy (CCFE), Culham Science Centre, Abingdon, Oxfordshire OX14 3DB, UK*

⁴ *Ecole Polytechnique Fédérale de de Lausanne (EPFL), Swiss Plasma Center (SPC), CH-1015 Lausanne, Switzerland*

⁵ *University of Seville, Spain*

[†] *See author list of H. Reimerdes et al 2022 Nucl. Fusion 62 042018*

A forward modeling technique is developed for determining the characteristic features of observed MHD modes from the line-of-sight data of the soft X-ray (SXR) diagnostics in the TCV tokamak. This technique can be used to evaluate the poloidal mode numbers m , radial location and ballooning character of the MHD modes. At the first stage the poloidal mode structures have been modeled by the radially localized Gaussian-shaped emission regions rotating along the magnetic flux surfaces. At the second stage, the space structure of observed 95-100kHz toroidal Alfvén eigenmode (TAE) are investigated numerically using HELENA, CSCAS and MISHKA codes. The calculated TAE eigenfunctions are used in our forward modeling similarly to the approach in contrast imaging diagnostics [Edlund E M *et al* 2009 *Phys. Rev. Lett.* **102** 165003]. A ballooning structure of the observed $n=1$ TAE mode can be analyzed due to low m in contrast to the high m modes analyzed by similar SXR technique in W7-X stellarator [M B Dreval *et al* 2021 *Plasma Phys. Control. Fusion* **63** 065006].

1. Introduction.

Optimization of the fast ions transport induced by MHD modes such as Alfvén Eigenmodes (AEs) is crucial for alpha-particle heating in future fusion reactors [1]. Knowledge of MHD modes structure and in particular toroidal Alfvén eigenmode (TAE) structure is important for this optimization.

A higher energy neutral beam injection (NBI) system was installed recently at the "Tokamak a Configuration Variable" (TCV) tokamak [2,3]. The TAEs and Energetic-Particle-Induced Geodesic Acoustic Modes (EGAMs) were observed during NBI heating on TCV [4]. Various high amplitude MHD modes in the frequency range up to 600 kHz were recently observed in TCV discharges with counter-current NBI injection [3]. Low frequency fraction of these modes is clearly seen by soft X-ray (SXR) cameras in addition to the magnetic diagnostics.

Data from SXR cameras are commonly used for studying spatial structures of MHD instabilities in magnetically-confined high-temperature plasmas. The analysis of the mode structure from the SXR raw data is not a straightforward one due to the line-of-sight integral nature of the SXR signals. The mode dynamics is usually observed as the poloidal propagation (in literature mostly called as "rotation") of plasma parameter perturbations. The perturbation crosses twice a line-of-sight

of SXR diagnostics during a full poloidal turn. In the SXR signals the impacts of positive and negative emissivity (emissivity below the average level) of the mode perturbations are combined. The various SXR data modeling can decode some properties of MHD modes from complex SXR signals. A spectral analysis of raw SXR signals can be used to determine the radial locations of MHD modes without tomographic inversion [5-9]. The poloidal mode number and radial location can be determined using a singular value decomposition (SVD) technique [5,7]. Forward modeling [5,10,11,12] can be used for this purpose as well.

The SXR intensity in a detector I_{SXR} defined by integrated along line of sight l and photon energies E of x-ray continuum emitted by Maxwellian plasma and filtered by a foil is :

$$I_{SXR} \propto \int_l \sum_i \frac{n_e n_i Z_i^2}{\sqrt{T_e}} \int_E e^{\frac{-E}{T_e} - \mu t} dE dl, \quad (1)$$

where n_e , n_i , Z_i , T_e are electron density, density, charge of ion with index i and electron temperature; μ, t are the absorption coefficients and thickness of a SXR-filtering foil [13]. The complex SXR signal dependence on the plasma parameters causes additional difficulties in MHD analysis.

The approach of using computed mode eigenfunctions can be implemented in forward modeling of line-integrated diagnostics [14]. A conventional technique of the AE modes description is based on the computation of their eigenfunctions, supported by plasma equilibrium reconstructed from external magnetic measurements and, if available, internal Motional Stark effect (MSE) measurements. This technique requires measurement of the safety factor and the plasma density profiles. In the framework of this technique, the mode structures are calculated numerically via linear MHD codes HELENA [15], CSCAS [16] and MISHKA [17] in our work. Cross-validation of the calculated plasma potential perturbations from these calculations and SXR forward modeling are used in our work.

A multiwire proportional soft X-ray (MPX) detector is used on the TCV tokamak as a high spatial resolution SXR emissivity imaging diagnostic [18]. The MPX system consists of 64 vertically viewing channels. These channels view the plasma core with a radial resolution of about 5 mm at the vacuum-vessel midplane, i.e., yielding a spatial resolution of 1% of the plasma diameter. The 50 μ m beryllium foil filter installed in MPX diagnostics cuts low energy emission and thus, allows monitoring SXR emission from the plasma core. The MPX signals were sampled at 200 kS/s sampling rate. This sampling allows studies of 95 kHz TAE mode.

The radial components of 3D magnetic sensors (three coils at the same position but with mutually perpendicular axes) [19] are used for the toroidal mode number determination in our work.

2. MHD activity in TCV discharges with counter-current NBI

Various 1-600 kHz modes were observed in counter-current NBI injection TCV discharges. An example of such modes is shown in Fig.1 for TCV discharge #71972.

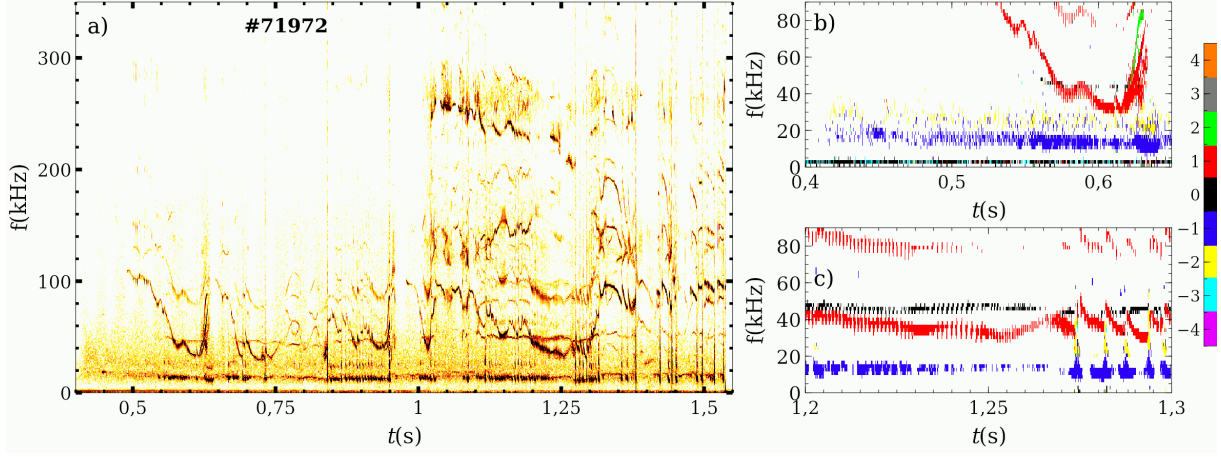


Figure 1. (a) The spectrogram of the LTCC coil signal in TCV pulse #71972 counter-injected NBI (b) and (c) The toroidal mode numbers n evaluated by radial -component magnetic LTCC coils.

Fast frequency evolution, such as frequency chirping indicate that even low frequency modes are fast-ion-driven modes. The $n=-1$ modes are propagated in the direction of NBI injection and opposite to the plasma current direction. A presence of substantial number of modes with positive n indicates that the fast ions distribution function is rather complex, and ions with negative and positive pitch-angles are present. One more example of counter-current NBI injection discharge is shown in Fig. 2.

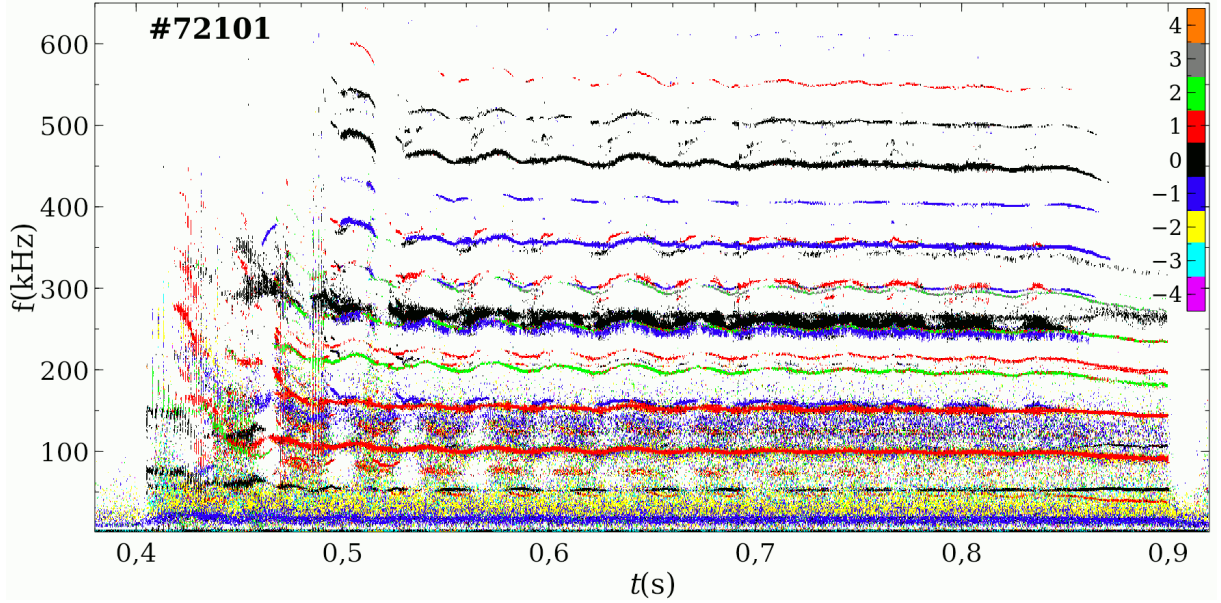


Figure 2. The toroidal mode numbers n evaluated by radial -component magnetic LTCC coils in TCV pulse #72101

Strong activity of MHD modes in wide frequency range indicates that the distribution function of fast ions can resonate with various modes in TCV discharges with counter-current NBI injection. Our work is concentrated on the space structure of some of these modes. These space structures can be used in further analysis, which is outside of our scope.

3. Forward modeling by the radially localized Gaussian-shaped emission regions

In order to extract information about the mode numbers and rotation direction from the line-integrated SXR measurement we use a simplified eigenmode model for the mode pattern in the poloidal plane of the location of the MPX camera (cf. Fig 3a) at the first stage. This model is adopted from the modeling and described in details in Ref.[12]. It is possible to perform “virtual measurement” along the lines-of-sight across the modeled X-ray radiation distribution. It is performed via the numerical integration for a given SXR camera geometry. The expected signals for a radiation distribution can be modeled by the numerical integration and compared with the measured signals. Fig. 3a represents, as an example, a modeled $m=2$ mode structure (color coded). The mode maxima and minima (blue color), consist of 2D Gaussians $\xi_i = \xi_{0i} \cdot e^{-(\vec{r}-\vec{r}_i)^2/\sigma^2}$ with their centers \vec{r}_i poloidally aligned on one of the magnetic flux surface. In this model, the constant background radiation distribution is assumed as subtracted, therefore, the negative radiation intensities can exist in the model.

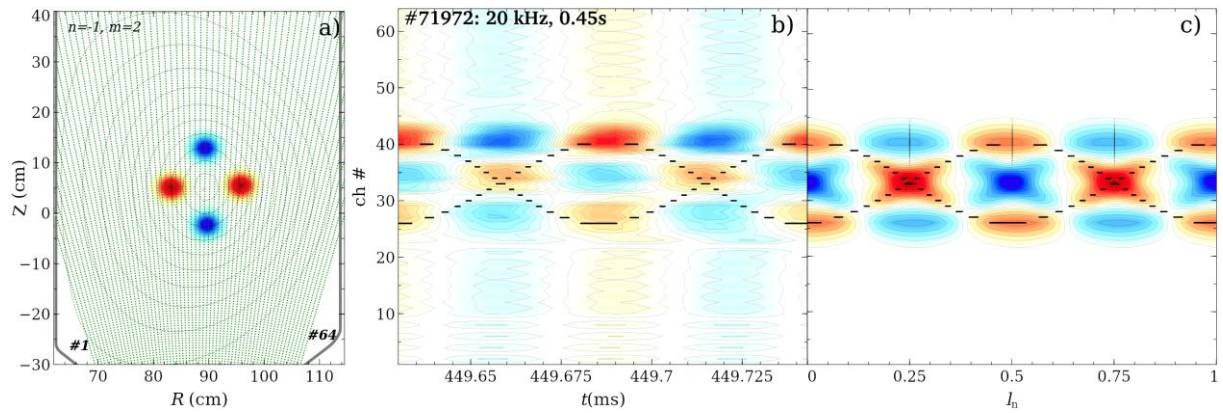


Figure 3. (a) Lines-of-sight of the MPX camera (green) across the magnetic flux surfaces are shown in black (#71972, 0.45s). A model radiation distribution of 4 Gaussian-shaped perturbations (of alternating positive and negative amplitudes, $\sigma=0.025$ m, color coded), representing an $m=2$ MHD mode located at $s \approx 0.3$. Spatiotemporal evolution of (b) experimental SXR emission data (#71972, 0.45s) measured by the MPX camera; a 25-25 kHz band-pass filter is applied to the data; numerical interpolation of the raw data of 64 diodes is used and (c) modeled data of the $m=2$ mode. The black lines indicate the mode path calculated for a thin mode ($\sigma=0.001$ m) for a single turn.

The experimental data of 20 kHz, $n=-1$ mode are shown as a contour plot in Fig.3b. The spatiotemporal evolution of the perturbation amplitude measured by the MPX camera is shown in the figure. The measured, bandpass-filtered perturbation amplitude is color-coded. Along the vertical axis the line-integrated MPX data are plotted against the time on the horizontal axis. Numerical interpolation of measured data is used in order to construct the SXR distribution along the cross-section on the base of 64 lines-of-sight.

As a first step radially thin perturbations ($\sigma=0.001$ m) are used to fit the experimentally observed paths of centers of the perturbations by variation of the mode number. The paths of two perturbations (i.e. mode maxima) are represented in Fig. 3 by the black lines. The poloidal movement of individual perturbations projected onto the detection plane of the camera leads to an apparent propagation in the opposite directions for perturbations near and faraway with respect to the camera. The poloidal mode number and radial mode location in the forward model are manually adjusted. In

order to compare these calculations with experimental data we perform the matching of two parameters: the initial phase and the rotation velocity. In our calculations in this section, the case of a constant poloidal rotation velocity is used. The path along the magnetic flux surface is used in our calculations for the poloidal mode velocity modeling. We use the normalized path l_n in our calculations [12]. The $l_n=1$ value corresponds to the single poloidal turn of the mode. Fig. 3c shows the effect of the radial mode perturbation width. A modeled $m=2$ mode having a wider perturbation size ($\sigma=0.025\text{m}$) is compared with the experimental data of Fig.3b. The modeling spatiotemporal evolution is in good agreement with the experimentally measured data. The $n=-1, m=2$ mode is located at $s=0.3$, where s is the square root of the normalized poloidal flux, i.e. $s = \psi_N^{1/2}$. The results of forward modeling of 40 kHz $n=1, m=3$ observed at 1.21s in #71972 are shown in Fig.4. The modeling results are similar to the experimental observation in this case as well.

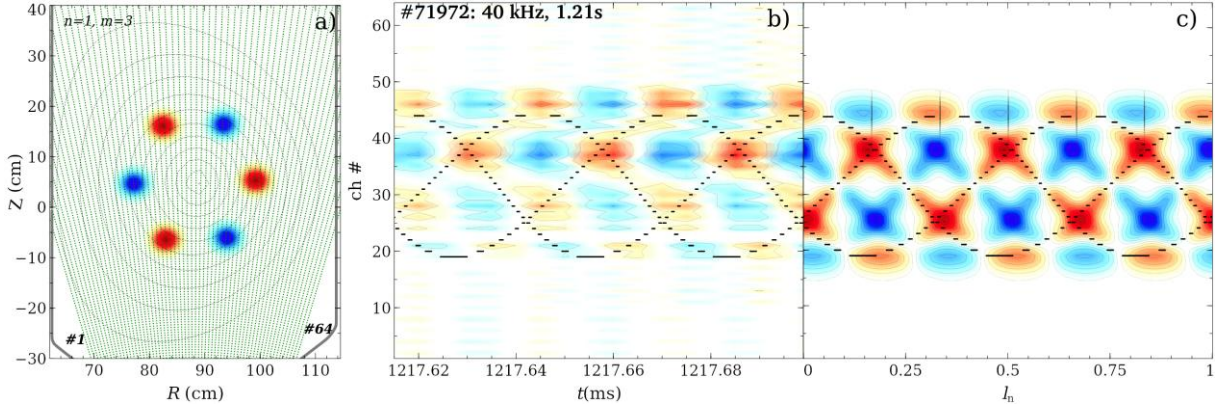


Figure 4. (a) A model radiation distribution of 6 Gaussian-shaped $\sigma=0.025$ m perturbations representing an $m=3$ MHD mode located at $s \approx 0.6$. Spatiotemporal evolution of (b) experimental SXR emission data (#71972, 1.21s) measured by the MPX camera; a 35-45 kHz band-pass filter is applied to the data; numerical interpolation of the raw data of 64 diodes is used and (c) modeled data of the $m=3$ mode. The black lines indicate the mode path calculated for a thin mode ($\sigma=0.001\text{m}$) for a single turn.

The results of forward modeling of 95 kHz $n=1, m=2$ observed at 0.88s in #72101 are shown in Fig.5. The current model of single m mode cannot describe the experimental observation in this case. Strong shift of the mode amplitude toward MPX channels with higher numbers is clearly observed. This shift corresponds to the shift of the mode pattern toward the low field side (LFS).

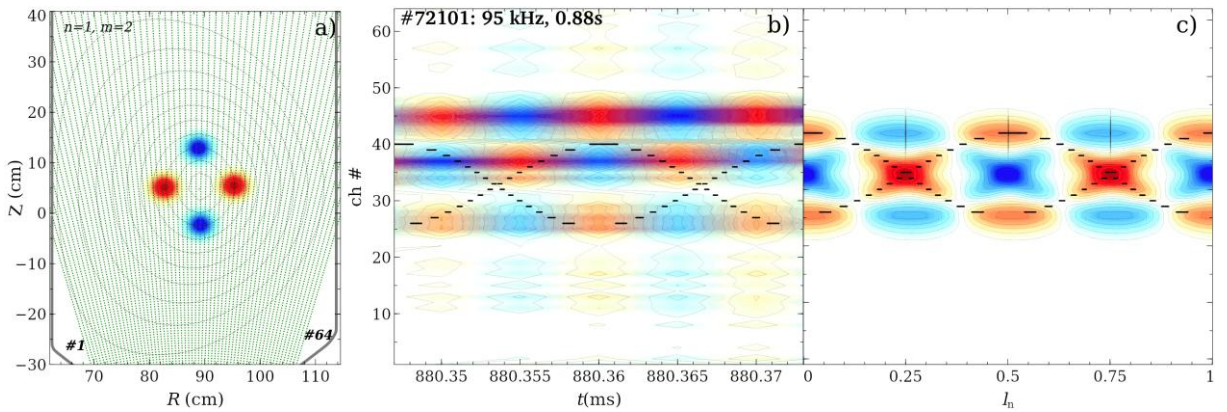


Figure 5. (a) A model radiation distribution of $m=2$ MHD mode located at $s \approx 0.3$. Spatiotemporal evolution of (b) experimental SXR emission data (#72101, 0.88s) measured by the MPX camera; a 90-100 kHz band-pass filter is applied to the data; numerical interpolation of the raw data of 64 diodes is used and (c) modeled data of the $m=2$ mode.

The modeling of single- m mode symmetric relatively to central MPX channel pattern as it is shown in Fig.5c. Thus, due to observed LFS shift this mode should contain more than one poloidal mode number. The LFS shift is typical for the ballooning modes. An analysis of multiple- m modes is difficult for the high m mode case [12]. As it is seen from Fig.5 such analysis is rather simple for low m TCV case. The spatiotemporal pattern is well fitted by $m=2$ modeling, except the LFS shift. This fact indicates that $m=2$ should be present as one of the multiple components of the multiple- m mode.

One more available experimental property of the modes under consideration is the time-averaged mode amplitude distribution [12]. It is expected that the perturbation interference in the case of multiple m modes should form different patterns of the time-averaged mode amplitude.

Distributions of the modes amplitude versus MPX channel is obtained from Fig.3-5 data by numerical integration of root mean squares of the data are shown in Fig.6 by green diamonds. One more parameter related to the time arranged amplitude of the mode, represented by a coherence of MPX data with the radial component magnetic data at the mode frequency. This coherence is shown in Fig.6 by blue squares.

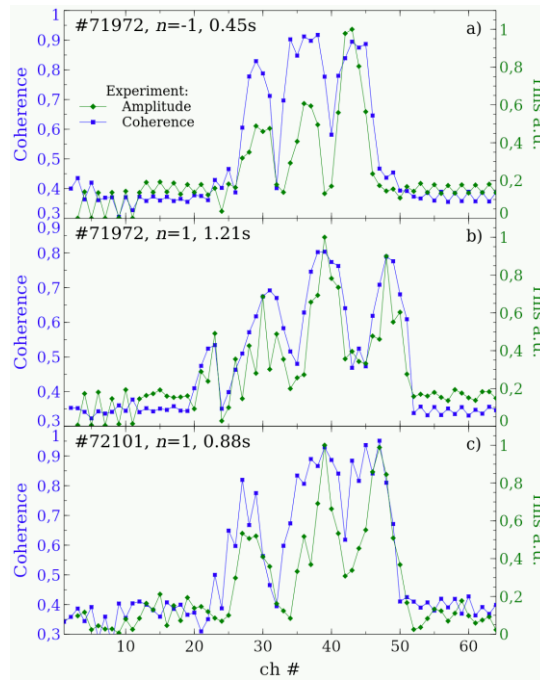


Figure 6. Distribution of rms of mode amplitude (in green) and coherence of MPX data to magnetic data (in blue) (a) #71972, 20khz, $n=-1$, 0.45s,(b) #71972, 40khz, $n=1$, 1.21s,(c) #72101, 95khz, $n=1$, 0.88s.

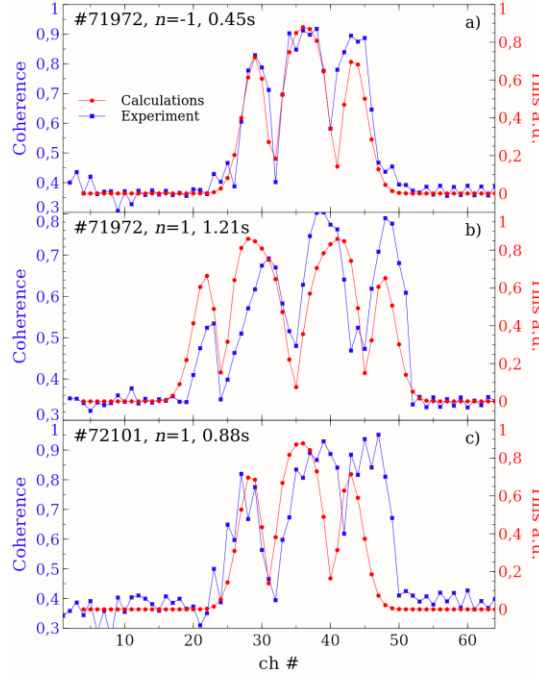


Figure 7. Distribution of coherence of MPX data to magnetic data (in blue) and calculated averaged amplitudes of the modeled mode structure (in red) (a) #71972, 20khz, $n=-1$, 0.45s,(b) #71972, 40khz, $n=1$, 1.21s,(c) #72101, 95khz, $n=1$, 0.88s.

The distribution of averaged amplitudes of calculated modes versus the MPX channel is shown in Fig.7 by red. In the case of high- m modes of W7-X uniform fluctuations amplitude distribution versus channel number was observed at the case of multiple- m modes[12]. In our low- m mode case, non-uniformity of the fluctuations amplitude distribution is observed in the case of #72101, 95khz, $n=1$, 0.88s, where multiple- m mode is expected. This effect can be explained by lower interference between mode perturbations in the low- m case. The results of forward modeling is in agreement with the experimental data for $n=-1$, $n=1$ modes of #71972, but contradict to #72101 data. Significant LFS shift of the mode amplitude is seen in #72101 from Figs.6,7 as well as from Fig.5.

4. MISHKA calculation of TAE eigenfunctions

A conventional technique of the MHD modes description is based on the computation of their eigenfunctions, on the base of external magnetic measurements. This technique requires measurement of the safety factor and the plasma density profiles. The AE mode structures are calculated numerically via linear MHD codes HELENA [15], CSCAS [16] and MISHKA [17] in our work. The summary of TAE calculations for #71972, $n=1$, 1.1s is present in Fig.8. The normalized frequency $\lambda = \omega R_0 / V_A = 0.263$ corresponds to lowermost TAE frequency about 135kHz. This frequency is above the 100kHz bandwidth of SXR diagnostics. The low frequency modes in #71972 are located well below TAE gap and can not be calculated via used codes.

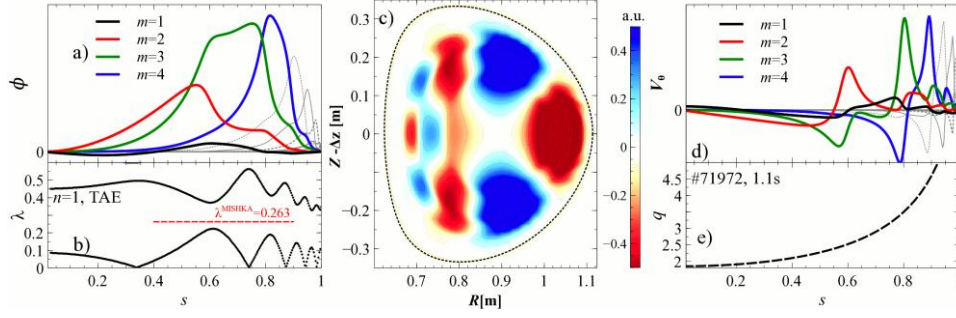


Figure 8. Calculated TAE modes: (a) plasma potential ϕ , (b) Alfvén continuum structures, (c) 2D structure of plasma potential ϕ , (d) poloidal velocity V_θ and (e) safety factor profile.

The TAE gap is substantially deformed and decreased in #72101 due to high value of the central safety factor in this discharge. Thus, the TAE gap frequency is located in 90-100kHz frequency range, below Nyquist frequency of MPX diagnostics. The summary of TAE calculations for #72101, 95kHz, $n=1$, 0.88s is present in Fig.9.

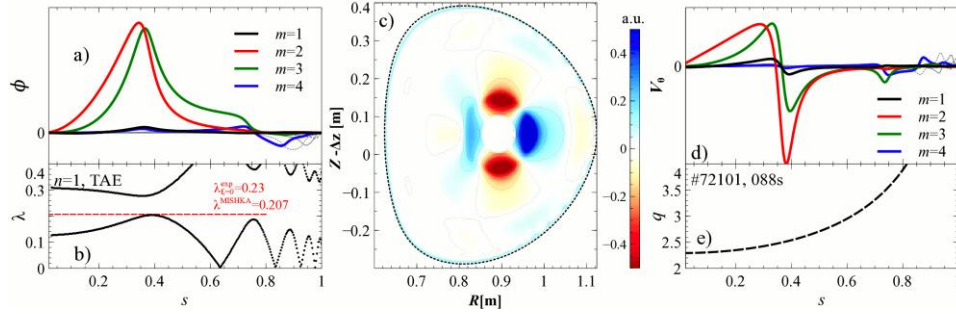


Figure 9. Calculated TAE modes: (a) plasma potential ϕ , (b) Alfvén continuum structures, (c) 2D structure of plasma potential ϕ , (d) poloidal velocity V_θ and (e) safety factor profile.

The wave perturbed electrostatic potential ϕ and poloidal velocity V_θ presented in this figure are estimated from the MISHKA output parameters as $\phi \sim sV_r/m$ and $V_\theta \sim (1/m)\partial(sV_r)/\partial r$. The result of simple estimation of the safety factor of TAE mode for $n=1, m=2$ TAE mode [20] $q=(m+0.5)/n=2.5$ coincides with our calculations.

5. Forward modeling using TAE eigenfunctions

In the framework of ideal MHD, used in our codes, plasma density perturbations are proportional to V_θ , and different to the plasma potential perturbations ϕ , as it is seen from Fig.9. The plasma perturbations shape is further deformed at the non-linear stage of a responsible instability. At the other side, the SXR emission perturbations are complicate function from plasma temperature and density perturbations, as following from Eq. (1). We are using TAE eigenfunctions of the plasma potential as an input data in our forward MHD modeling. A comparison of the spatiotemporal evolution of the perturbation amplitudes measured by MPX diagnostics with the spatiotemporal evolution of numerical integration of $n=1$ TAE eigenfunctions at single poloidal turn are shown in Fig.10.

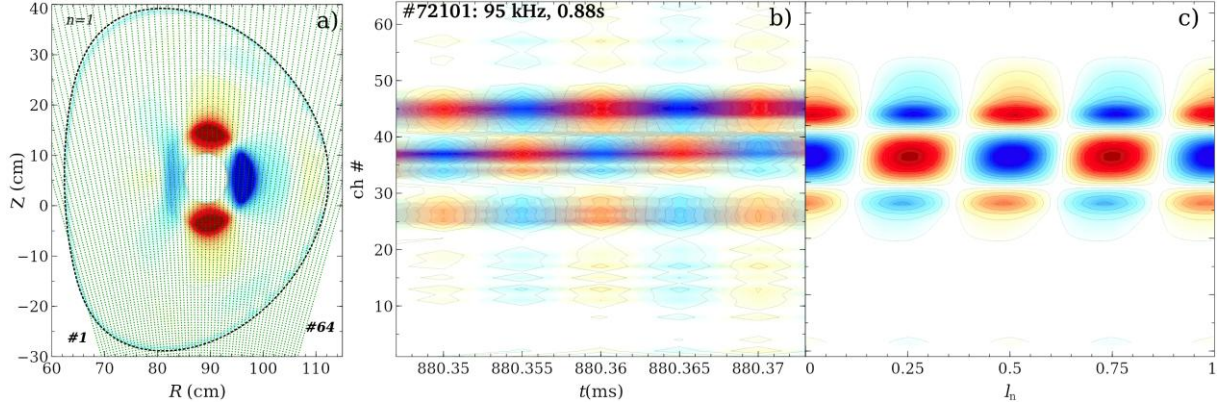


Figure 10. (a) A model radiation distribution of MHD mode from TAE eigenfunctions. Spatiotemporal evolution of (b) experimental SXR emission data (#72101, 0.88s) measured by the MPX camera; a 90-100 kHz band-pass filter is applied to the data; numerical interpolation of the raw data of 64 diodes is used and (b) modeled data .

Shapes and positions versus SXR channels of the experimental spatiotemporal phase diagram Fig.10(b) and modeled one are quite similar in contrast to simplified modeling of Fig.5. Good agreement in the spatiotemporal phase diagrams demonstrates cross-validation of two techniques: conventional technique, based on the determination of the toroidal mode number n from magnetic measurements with further numerical calculations of m and our forward modeling technique. Observed LFS shift of the SXR emission pattern represents ballooning nature of the TAE mode. Good agreement is also seen from time-averaged distribution of TAE mode as it is shown in Fig.11.

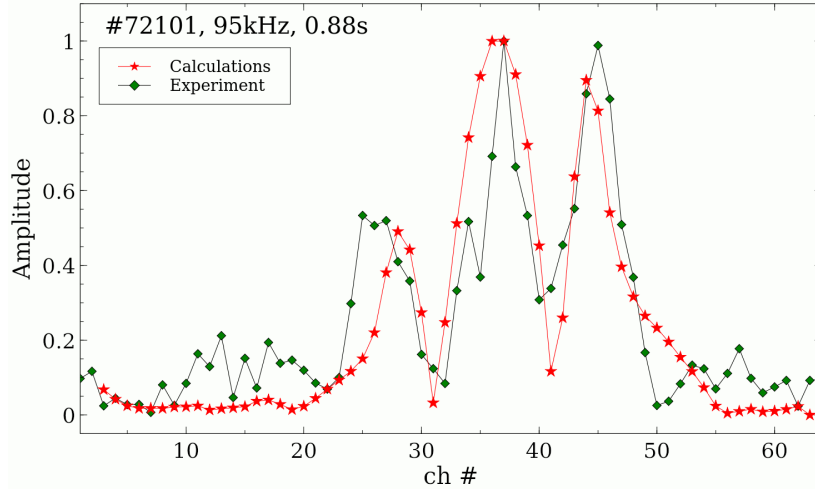


Figure 11. Distribution of rms of mode amplitude (green diamonds) from Fig. 6 and calculated via TAE eigenfunctions averaged amplitudes of the modeled mode structure from #72101, 95kHz, $n=1$, 0.88s.

The experimentally observed LFS shift is well reproduced by the eigenfunctions-based modeling, in contrast to the simplified modeling, as it is seen from Fig.11 and Fig.7c correspondently.

The distribution of amplitude of normalized temperature $\delta T_e/T_e$ and density $\delta n_e/n_e$ fluctuations show substantially higher amplitude at high field side (HFS) [20,21] in the case of symmetric pattern of the potential ϕ fluctuations. Since the SXR signal fluctuations contains complex dependence from plasma

parameters, we cannot consider ratio of HFS to LFS amplitudes of the the SXR fluctuations for the ballooning mode character discrimination. However, we can consider positions of the SXR signal peaks versus channel number. The considerable LFS shift of the mode confirm the ballooning character of the TAE mode.

6. Conclusions

A forward modeling technique is developed for determining the characteristic features of observed MHD modes from the line-of-sight data of the soft X-ray (SXR) diagnostics in the TCV tokamak. This technique was used to evaluate the poloidal mode numbers m , radial location and ballooning character of the MHD modes. At the first stage the poloidal mode structures have been modeled by the radially localized Gaussian-shaped emission regions rotating along the magnetic surfaces. At the second stage, the space structure of observed 95-100kHz toroidal Alfvén eigenmode (TAE) are investigated numerically using HELENA, CSCAS and MISHKA codes. The calculated TAE eigenfunctions are used in our forward modeling. Various high amplitude 1-700kHz modes are observed in TCV discharges with counter-current NBI injection. The $n=-1$, 20 kHz mode at 0.45s of #71972 has been recognized as $m=2$ and localized at $s\approx 0.3$. The $n=1$, 40 kHz mode at 1.21s of #71972 has been recognized as $m=3$ and localized at $s\approx 0.6$. The $n=1$, 95 kHz mode at 0.88s of #72101 has been determined as TAE mode according to the linear-MHD code MISHKA. The calculated TAE eigenfunctions were used as an input for the forward modeling of the line-integrated SXR data fluctuations. The results of the modeling agree with the experimental data. The ballooning TAE with dominant poloidal harmonics $m=2, m=3$ is located at $s\approx 0.3-0.4$ is recognized by our modeling. The modes space structures obtained in the present work can be used in further MHD modes analysis in TCV.

Acknowledgments

This work has been carried out within the framework of the EUROfusion Consortium, funded by the European Union via the Euratom Research and Training Programme (Grant Agreement No 101052200 — EUROfusion). Views and opinions expressed are however those of the author(s) only and do not necessarily reflect those of the European Union or the European Commission. Neither the European Union nor the European Commission can be held responsible for them. This work was supported in part by the Swiss National Science Foundation.

References

- [1]] A. Fasoli *et al* 2007 *Nuclear Fusion* **47** S264
- [2] S. Coda *et al* 2017 *Nucl. Fusion* **57** 102011

- [3] M. Vallar *et al* Proc of 48th EPS Conference on Plasma Physics
- [4] B Geiger *et al* 2020 *Plasma Phys. Control. Fusion* **62** 095017
- [5] Weller A *et al* 2007 *Proc of 34th EPS Conference on Plasma Physics* P1.112
http://epsppd.epfl.ch/Warsaw/pdf/P1_112.pdf
- [6] Razumova K A *et al* 2003 *Plasma Phys. Control. Fusion* **45** 1247
- [7] Igochine V, Günter S, Maraschek M, and the ASDEX Upgrade Team 2003 *Nucl. Fusion* **43** 1801
- [8] Weiland M *et al* 2015 *Plasma Phys. Control. Fusion* **57** 085002
- [9] Franz P *et al* 2004 *Phys. Rev. Lett.* **92** 125001
- [10] Dreval M B *et al* 2016 *Rev. Sci. Instrum.* **87** 073503
- [11] Dreval M *et al* 2011 *Rev. Sci. Instrum.* **82** 053503
- [12] M B Dreval *et al* 2021 *Plasma Phys. Control. Fusion* **63** 065006
- [13] S Morimoto *et al* 1986 *Japanese Journal of Applied Physics* **25** 120
- [14] Edlund E M *et al* 2009 *Phys. Rev. Lett.* **102** 165003
- [15] Huysmans G.T.A. *et al* 1991 *International Journal of Modern Physics C* **02(01)** 371
- [16] Kerner W. *et al* 1998 *J. Comput. Phys.* **142** 271
- [17] Mikhailovskii A.B. *et al* 1997 *Plasma Phys. Rep.* **23** 841
- [18] A. Sushkov *et al* 2008 *Review of Scientific Instruments* **79** 023506
- [19] D. Testa *et al* 2015 *Fusion Engineering and Design* **96-97** 989
- [20] R. M. Nazikian *et al* 2003 *Phys. Rev. Lett.* **91** 125003
- [21] M. A. Van Zeeland *et al* 2006 *Phys. Rev. Lett.* **97** 135001